

Water Conservation & Management (WCM)

DOI: http://doi.org/10.26480/wcm.03.2025.574.582



ISSN: 2523-5672 (Online) CODEN: WCMABD RESEARCH ARTICLE

BIOMASS-DERIVED $rGO-TIO_2$ COMPOSITE FOR SUSTAINABLE WASTEWATER TREATMENT VIA DUAL PHOTOCATALYTIC DEGRADATION AND REDUCTION PATHWAYS

Dessy Ariyantia,b,c*, Dina Lesdantinaa,b,c, Aprilina Purbasaria,b, Wei Gaod

- ^aDepartment of Chemical Engineering, Faculty of Engineering, Universitas Diponegoro, Tembalang, Semarang, INDONESIA
- bCenter of Advanced Materials for Sustainability, Faculty of Engineering, Universitas Diponegoro, Tembalang, Semarang, INDONESIA
- cSDGs Center Universitas Diponegoro Tembalang, Semarang, INDONESIA
- ^aDepartment of Chemical and Materials Engineering, The University of Auckland, Auckland 1142, New Zealand
- *Corresponding Author Email: dessy.ariyanti@che.undip.ac.id

This is an open access journal distributed under the Creative Commons Attribution License CC BY 4.0, which permits unrestricted use, distribution, and reproduction in any medium, provided the original work is properly cited

ABSTRACT

Article History:

Received 11 June 2025 Revised 21 July 2025 Accepted 17 August 2025 Available online 04 September 2025 Heavy metals and organic dyes present in industrial wastewater pose significant risks to human health and the environment. Among available treatment methods, the advanced oxidation process (AOP) has gained attention for its ability to achieve complete degradation and removal of such contaminants. This study aims to synthesize a TiO2-reduced graphene oxide (rGO) composite and evaluate the role of each component in the combined adsorption-desorption and photocatalytic degradation mechanisms. The rGO was derived from agricultural waste—sugarcane bagasse and coconut shell—and combined with TiO2 via a hydrothermal method. The resulting composites, C-SB (from sugarcane bagasse) and C-CS (from coconut shell), $demonstrated\ effective\ removal\ of\ Cu(II)\ and\ methylene\ blue\ (MB).\ C-SB\ achieved\ removal\ efficiencies\ of\ 87\%$ for Cu(II) and 46% for MB, slightly outperforming C-CS with 76% and 44%, respectively. TiO_2 exhibited a dominant photocatalytic effect in MB degradation, while rGO primarily facilitated Cu(II) removal through adsorption. The adsorption-desorption phase was found to significantly influence the photocatalytic efficiency. Kinetic analysis indicated that a pseudo-first-order model best described the MB adsorptiondesorption process $(R_2 = 1)$, while a first-order kinetic model effectively represented the photocatalytic degradation, with R2 values of 98.68% for C-SB and 95.67% for C-CS. These findings highlight the potential of TiO2-rGO composites, especially those derived from sugarcane bagasse, in treating complex wastewater through a synergistic mechanism of adsorption and photocatalysis.

KEYWORDS

 $adsorption, rGO, biomass, photocatalysis, photodegradation\ kinetics$

1. Introduction

Various inorganic and organic pollutants in industrial wastewater may threaten the aquatic environment. The use of heavy metal Cu (II) in various technologies such as in the medical, agricultural, and other industrial fields as well as organic pollutants such as dyes in the textile, paper, leather, food, and cosmetics industries can generate polluted wastewater that may interfere with marine life, lead to eutrophication, cause fish mortality, and even have the potential to enter the human food chain, which can lead to various serious diseases such as seizures, lung and nervous system damage (Chaabane, et al., 2020; Ariyanti, et al., 2018). Cu (II) can cause negative effects as it is toxic, non-degradable, and easily accumulates (Yu, et al., 2000). The maximum safe limit for Cu (II) metal in drinking water is 0.05 mg/L (Tomczyk, et al., 2020). Dyes produced from industrial waste are also generally carcinogenic and toxic.

Several conventional methods have been applied to reduce wastewater pollution, including chemical precipitation, solvent extraction, ion exchange, membrane filtration, coagulation, and electrochemistry. However, the use of the methods has several shortcomings, including imperfect absorption, the amount of energy used, low efficiency, sensitive operating conditions, and toxic sediment (Burakov, et al., 2018). The

oxidation process at a higher level better known as the advanced oxidation process (AOP) is a technology that is being developed to degrade organic and inorganic pollutants both in water and air. This process can be characterized by the production of hydroxyl ions (OH) and superoxide (O2), which are highly reactive to break down undissolved organic and inorganic pollutants. Photocatalysis is one part of the AOP method that is currently attracting attention because the process is environmentally friendly, utilizing unlimited solar energy for catalyst activation. TiO2 has been widely recognized as a functional ingredient in semiconductor photocatalysis and is widely used to degrade environmental pollutants in both air and water. Some of the advantages of using TiO2 include low cost, non-toxicity, high chemical stability, and good reactivity to light, but this material has a large band gap (Ariyanti, et al., 2017; Ariyanti, et al., 2022).

On the other hand, reduced graphene oxide (rGO) is a material, a derivative of graphene that has unique chemical, optical, and electrical properties because it is composed of a graphene framework and contains an oxygen functional group (Guerrero-Contreras, et al., 2015; Ariyanti, et al., 2021). rGO has been widely applied in various technologies, including biosensors, drug delivery, nanoelectronics, energy storage, supercapacitors, and catalysts in waste management (Seekaew, et al., 2018). rGO has good adsorption properties and has the potential to be

Quick Response Code

Access this article online



Website: www.watconman.org DOI:

10.26480/wcm.03.2025.574.582

used as supporting material for the photocatalytic process if it is combined with other materials that have high photocatalytic activity such as TiO_2 (Ariyanti, et al., 2023; Lesdantina and Ariyanti, 2020). Research stated that a combination of rGO derived from graphite and TiO_2 is proven to produce better performance as a photocatalyst when compared to using only rGO or TiO_2 (Zhang, et al., 2010).

The existence of rGO with its special characteristics has considerable potential for further development. The synthesis process with various raw materials has not been developed widely as rGO is mostly produced from graphite as raw material. Biomass-derived materials have gained considerable attention as sustainable and renewable carbon sources for the synthesis of advanced carbon nanomaterials such as reduced graphene oxide (rGO). Utilizing biomass not only provides an environmentally friendly approach but also adds value to agricultural and industrial waste products. Various biomass resources, including wood charcoal, sawdust, coconut shell, bagasse, rice husks, used tires, polymer, and cellulose-based waste have been explored for their potential to serve as precursors for rGO synthesis (Lee, et al., 2019).

In this work, sugarcane bagasse and coconut shell biomass were selected due to their high carbon content, wide availability, and low cost. In addition, the reaction mechanism and reaction kinetics in the photocatalytic process of $rGO-TiO_2$ composites in reducing Cu (II) as an inorganic pollutant and degrading MB dye as an organic pollutant also investigated to find out the role of rGO in $rGO-TiO_2$ composites for synergetic adsorption-desorption and photocatalytic process.

2. MATERIALS AND METHODS

2.1 Materials

The raw materials used to produce rGO were sugarcane bagasse and coconut shells, both sourced from the local market in Semarang, Indonesia. Tetra-n-butyl-titanate ($\text{Ti}(OC_4H_9)_4$, 97% purity, liquid form) was used as the $\text{Ti}O_2$ precursor and imported from Qingdao, China. Other chemicals employed included sulfuric acid (H_2SO_4 , 98% concentration, liquid form, Merck), potassium permanganate (KMnO₄, ≥99% purity, crystalline solid, Merck), hydrogen peroxide (H_2O_2 , 30% w/w concentration, aqueous solution, Merck), and ethanol (C_2H_5OH , ≥99.8% purity, liquid form, Merck), along with distilled and deionized water. Prior to further processing, the biomass was charred in a furnace at 260 °C for 30 minutes and subsequently ground into fine particles. All chemicals were of analytical reagent (AR) grade and were used without further purification.

2.2 Synthesis of Reduced Graphene Oxide

rGO was synthesized by a modified Hummers method (Ariyanti, et al., 2023; Guerrero-Contreras, et al., 2015; Muramatsu, et al., 2014). A total of 5 g of charred biomass was dispersed in 125 mL of concentrated sulfuric acid (98%) while being maintained in an ice bath. Potassium permanganate (15 g) was then gradually added to the mixture with continuous stirring, ensuring the temperature remained below 20°C. The reaction mixture was subsequently transferred to a water bath, where the temperature was controlled between 35-40°C and stirred for 3 hours. Initially, upon the addition of KMnO4, the solution appeared blackish purple. Over time, it turned greenish black, indicating the formation of dimanganese heptoxide due to the reaction between sulfuric acid and potassium permanganate. Next, 100 mL of deionized water was slowly introduced, as its addition could generate bubbles and cause a rapid increase in temperature. The temperature was then maintained at 95°C for 15 minutes. During this stage, the solution's color changed to yellowish brown. Another 100 mL of deionized water was added, followed by the gradual addition of 25 mL of hydrogen peroxide (30%) to eliminate any remaining potassium permanganate. The solution changed from light or dark brown to bright yellow. The resulting material was filtered under warm conditions and repeatedly washed with distilled water until the pH reached neutral. The solid residue was then dried in an oven at 80°C for 6 hours. The dried sample was subsequently ultrasonically exfoliated in a 50 kHz ultrasonic bath (Krisbow) for 30 minutes after being dispersed in deionized water. Samples were labeled C-SB and C-CS for sugarcane bagasse and coconut shell, respectively.

2.3 Synthesis of rGO-TiO₂ Composite

 $4\,$ ml of tetra-n-butyl-titanate (TNBT) as a base for making TiO_2 was dissolved in 20 ml of ethanol and stirred using a magnetic stirrer for 30 minutes. 10 mg of rGO was dissolved in 10 ml of deionized water and treated in an ultrasonic bath (Krisbow, 50kHz) for 30 minutes. The rGO solution was then added to the TiO_2 solution made from TNBT and stirred for 1 hour to form a homogeneous suspension. The suspension was placed in a 40 ml Teflon-sealed autoclave and maintained at 120°C for 3 hours, after which TiO_2 deposition on the carbon substrate, rGO was obtained.

The composite was filtered and rinsed using deionized water several times and dried at room temperature (Baorang, et al., 2002).

2.4 Characterization

The crystal structure of the sample was studied using SHIMADZU XRD-7000 by packing the dried sample on a glass sample plate and scanning from 2 theta 10-60 degrees. Fourier transform infrared spectroscopy (FTIR) was conducted in the wave number range of 4000-400 cm $^{\rm 1}$ using PerkinElmer Spectrum IR 10.6.1 to observe the chemical bonding of the samples. Scanning Electron Microscope (SEM) 20 kV was used to identify the morphology of the rGO-TiO2 composite.

2.5 Adsorption-Photocatalysis Performance

The photocatalytic activity of $rGO-TiO_2$ composites in Cu (II) metal content reduction was evaluated by measuring the remaining Cu (II) concentration in the solution after the adsorption photocatalysis process for the representation of inorganic pollutant removal from the water. First 5 ppm of Cu (II) solution (100 mL) was prepared by adding $CuSO_4$ into distilled water followed by the addition of 1 g/L composite catalyst into the solution. The solution was stirred at 150 rpm for 30 minutes in a dark condition before the photocatalysis process. Adsorption was carried out at pH 7 and room temperature. The photocatalysis was conducted by irradiating the solution while stirring with UV light (20 W; 254 nm), with the distance between the sample and the UV lamp about 30 cm for 120 min. The sample was taken 15 ml every 15 minutes for further analysis using Atomic Absorption Spectrophotometry (AAS) with a wavelength of 324,75 nm to measure the remaining Cu (II) concentration in the solution.

Meanwhile, the organic pollutant degradation performance of the rGO-TiO₂ composite was also observed through the adsorption-photocatalysis of methylene blue (MB) in the aqueous solution. Following the same procedure as Cu (II), the 100 mL 5 ppm MB solution was mixed with 1 g/L $\,$ composite and placed in the photocatalytic chamber that consisted of a 20 W UV lamp with a 30 cm distance. An initial 30-minute stirring step was conducted in the absence of light to facilitate adsorption on the catalyst surface. After this dark adsorption period, the photocatalytic process was initiated and maintained for 120 minutes under light exposure. During the reaction, 15 mL of the solution was withdrawn every 15 minutes for analysis. The concentration of methylene blue in each sample was determined using a UV-Vis spectrophotometer at a wavelength of 665 nm. The selection of a catalyst dosage of 1 g/L and a pollutant concentration of 5 ppm was based on the results of our preliminary experiments as well as a summary of findings from the literature review. The amount of photoreduction metal C_t/C_0 Cu (II) and photodegradation of MB is expressed in, where Ct is the concentration of pollutants after the photocatalytic reaction and C_0 is the initial concentration of pollutants before the reaction occurs (Zhang Yanhui, et al., 2010).

2.6 Reaction Kinetics Model

2.6.1 Adsorption and desorption reaction kinetics

Adsorption performance is significantly influenced by the adsorption ability and electron-hole transport. The model used follows the Langmuir model, where the number of pollutants adsorbed at time t is calculated according to the following equation (Ding, et al., 2019) :

$$qt = \frac{(c_0 - c_t)V}{m} \tag{1}$$

Where C_0 and C_t (mol/L) are the initial concentrations and the concentration at a given time; V is the volume of the solution containing the pollutant (L); qt (mg/g catalyst) and m is the mass of the catalyst (g). The adsorption capacity under equilibrium conditions (qe) and the adsorption rate constant (k) are usually estimated by the pseudo-first and second-order equations, and the appropriate value is chosen based on the higher correlation coefficient R^2 . The kinetics of the pseudo-first-order with linear form the following equation:

$$ln(q_e - q_t) = ln \, q_e - k_1 t \tag{2}$$

The k_1 and q_e values can be obtained from the slope and intercept values by fitting data ln (qe - qt) vs t. As for the nonlinear form, it follows the equation below:

$$q_t = q_e (1 - e^{-k_1 t}) (3)$$

where q_e and q_t are the adsorption capacity at a certain equilibrium and time (mg/g catalyst), t (min) is the reaction time and k_1 (1/min) is the pseudo-first-order rate constant.

The pseudo-second-order kinetics is used based on the adsorption equilibrium capacity with the linear form of the following equation:

$$\frac{t}{q_t} = \frac{1}{k_2 q_e^2} + \frac{1}{q_e} t \tag{4}$$

Where k_2 is the second-order pseudo rate constant (g catalyst/mg.min). The values of qe and k_2 are determined from the slope and intercept by fitting data t/qt vs t.

2.6.2 Photocatalytic reaction kinetics

The photodegradation process of MB follows the first-order Langmuir-Hinshelwood (L-H) model which is described by the following equation:

$$r = \frac{dC}{dt} = \frac{k_{app}KC}{1+KC} \tag{5}$$

where C is the concentration of MB, k is the degradation rate constant and K is the adsorption constant at equilibrium. Since it is independent of concentration, the apparent rate constant has been selected as the fundamental kinetic parameter for comparing the various systems. This allows one to ascertain the photo-catalytic activity without reference to the duration of the preceding adsorption in the dark. The reaction speed can be simplified to equation 6.

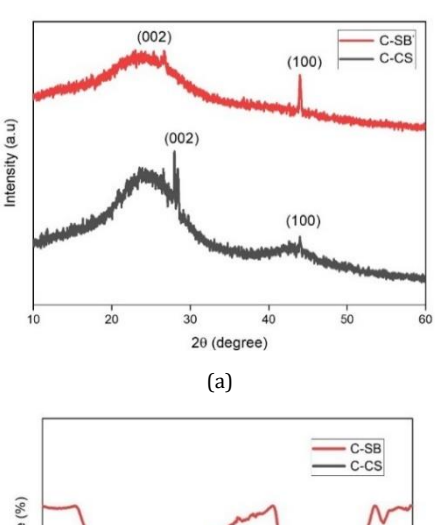
$$\ln C/_{C_0} = -k_{app}t \tag{6}$$

where C is the concentration of MB at a certain time, C_0 is the initial concentration, k_{app} is the apparent rate constant and t is time.

3. RESULTS AND DISCUSSIONS

3.1 Characterization

Based on Figure 1, the diffraction pattern samples from bagasse produce a wider peak at $2\theta=26,5^\circ$ and a low peak intensity at $2\theta=44^\circ$. Li, et al., 2018 state that the diffraction pattern at 26,5° is related to graphite or the possibility of the formation of reduced graphene oxide (rGO) (Li, et al., 2018). The van der Waals bond between two adjacent layers which is more dominant than the bond with the oxygen functional group on the surface allows the formation of piles between layers again so that the resulting product characteristics are more like pure graphite or reduced graphene oxide (rGO) (21). Based on the shape of the wider peak in the graphitic plane (002) with an angle of $2\theta=26,5^\circ$ and low intensity at the peak (100) with an angle of $2\theta=44^\circ$, the samples produced from bagasse are more likely to have characteristics similar to reduced graphene oxide (22).



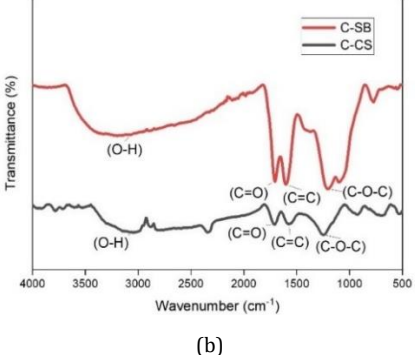


Figure 1: (a) XRD pattern and (b) FTIR analysis of rGO synthesized from bagasse (C-SB) and coconut shell (C-CS)

Samples from coconut shells show a diffraction pattern with a wider range at $2\theta = 23.7^{\circ}$ - 28.18° . The peak which is a graphical plane labeled (100) is also seen at an angle of $2\theta = 43.8^{\circ}$. Based on research by Sujiono et al. two

dominant peaks at $2\theta = 23,97$ ° and 43,04° indicate that the sample formed is reduced graphene oxide (rGO)(23). Thus, the sample synthesized by the modified Hummers method made from coconut shell as a raw material of this study is reduced graphene oxide (002). This is also reinforced by the results of research by Emiru et.al which confirmed that the diffraction peak at $2\theta = 23,8$ ° is reduced graphene oxide (Emiru, et al., 2017).

rGO produced from coconut shell contains functional groups including C-O stretching with a peak of $\sim 1245~\text{cm}^{-1}$, C = C at a peak of $\sim 1575~\text{cm}^{-1}$ which is a graphite domain that is not oxidized, C=O is shown at the peak of $\sim 1715~\text{cm}^{-1}$, while in the range of $\sim 3045~\text{cm}^{-1}$, there is a wide enough curve and the peak formed confirms the presence of O-H. The overall oxygen functional groups contained in the sample show the characteristics of rGO (Baqiya et al., 2020). FTIR analysis for samples made from bagasse showed a widened indentation with a peak of $\sim 3201~\text{cm}^{-1}$ which indicates O-H stretching of a hydroxyl group. The narrower peaks at $\sim 1705~\text{cm}^{-1}$ and $\sim 1602~\text{cm}^{-1}$ represent C=O and C = C. The presence of peaks at the wavelengths of $\sim 1204~\text{cm}^{-1}$ and $\sim 1094~\text{cm}^{-1}$ indicate C-O stretching. The low intensity of the indentation containing the oxygen functional group on the sample occurs due to de-oxygenation which indicates the formation of reduced graphene oxide (Li, et al., 2018).

Characterization using XRD analysis aims to study the crystal structure so that the crystal phase in the composite which is synthesized via the hydrothermal method can be identified. RGO-TiO₂ composite that was synthesized using rGO from bagasse was labeled C-SB while using coconut shell was labeled C-CS and the diffraction peak result can be seen in Figure 2. The diffraction peak of the C-SB composite was at $2\theta = 25,29^{\circ}$; $37,88^{\circ}$; $47,88^{\circ}$; $54,4^{\circ}$, while in C-CS exhibited $2\theta = 25,30^{\circ}$; $37,97^{\circ}$; $47,79^{\circ}$; $54,38^{\circ}$ with indexes (101), (004), (200), (211), and (204). All peaks identified, showed peaks resembling TiO₂ anatase with $2\theta = 25,18^{\circ}$; $37,62^{\circ}$; $48,2^{\circ}$; $54,34^{\circ}$ (JCPDS 21-1727). The widening peak occurs due to the addition of rGO in the composite.

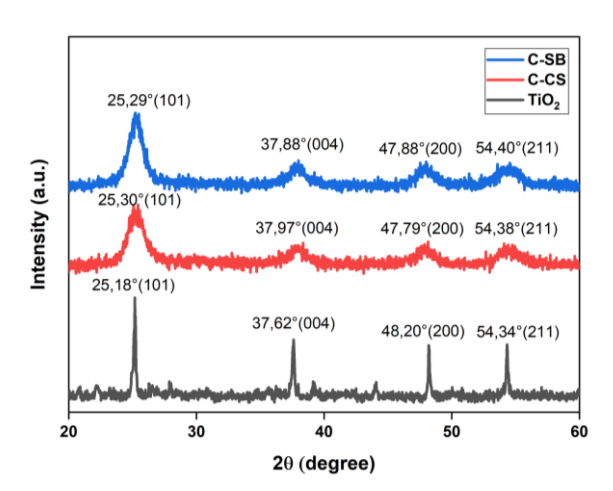
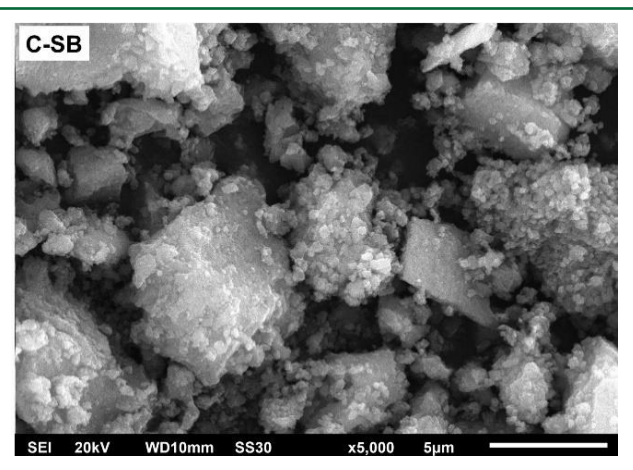


Figure 2: XRD of TiO₂ and rGO-TiO₂ composite with the addition of rGO from sugarcane bagasse (C-SB), and coconut shell (C-CS)

This is the same with the XRD results of rGO which showed a wide peak at $2\theta=26.5$ ° for rGO from bagasse and $2\theta=23.7$ ° - 28.18° for rGO synthesized from coconut shell. The diffraction peaks that resemble TiO_2 anatase occur because the amount of rGO added during the synthesis process tends to be less, so the rGO peaks are not visible due to overlapping with the peaks of TiO_2 anatase (Kusiak-Nejman, et al., 2020). The synthesis process can also cause low intensity of rGO which occurs due to disruption of the regular stack on the rGO sheet because of intercalation with the presence of TiO_2 (Sharma, et al., 2018).

SEM result as shown in Figure 3 depicted the attachment of TiO_2 on rGO surface. In C-SB composites, the presence of rGO in the sheet form is still visible, where the surface covered by TiO_2 , is either still spherical or forms a larger size due to agglomeration.



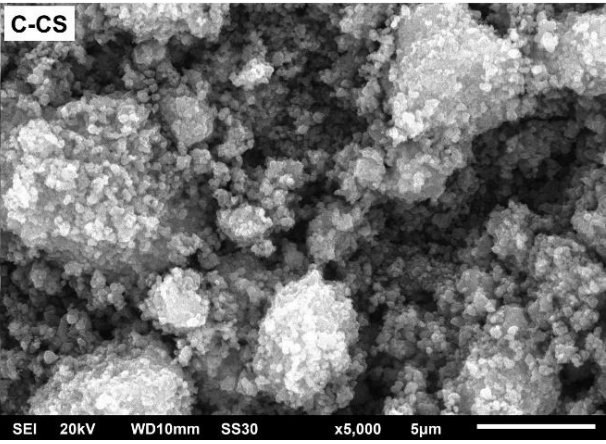


Figure 3: SEM of rGO-TiO₂ composite with the addition of rGO from sugarcane bagasse (C-SB), and coconut shell (C-CS)

The presence of TiO_2 on the rGO surface causes the separation of layers of rGO sheets to form a sandwich-like structure where the TiO_2 is between the rGO sheets. The distribution of TiO_2 on the rGO surface is uneven, where there are parts of rGO that are filled with TiO_2 , but there are also surfaces that are completely unattached by TiO_2 . Meanwhile, in the C-CS composite, the rGO sheet is not visible at all. This occurs because the TiO_2 agglomeration with a larger size sticks to the rGO surface. However, the spherical shape of TiO_2 is still visible even though this compound tends to form agglomeration. This indicates that the hydrothermal process in the synthesis of rGO- TiO_2 composites only slightly affects the morphological shape of TiO_2 (Sharma, et al., 2018).

3.2 Photocatalysis for inorganic pollutant removal

To determine the role of rGO in the photocatalytic process of inorganic and organic pollutants, rGO, which has undergone a hydrothermal process forms an rGO-TiO $_2$ composite, used as a photocatalyst. As the controlled standard, TiO $_2$ synthesized from TNBT is also used as a catalyst in the degradation process.

Based on Figure 4, the concentration of Cu (II) has decreased significantly during the adsorption process. The decrease in Cu (II) concentration using C-SB was 87% and 76% for C-CS. Both catalysts show better adsorption ability than TiO2. During the first 30 minutes of irradiation or the beginning of the photocatalytic process, a decrease in Cu (II) concentration occurred with the use of C-CS with a decrease of 23%, but in the next minute, the Cu (II) concentration tended to increase. The amount of Cu (II) that is adsorbed causes most of the active sites rGO to be filled, so when the irradiation process, the electrons from the TiO2 conduction band will occupy the remaining active site of rGO then react with O_2 to form superoxide radicals which are used to reduce Cu (II) remaining in solution. However, this photocatalytic process did not last long because rGO surface was fully charged, causing the electrons in the TiO2 conduction band not to be adsorbed on the rGO surface and to tend to recombine with holes in the valence band, so that the Cu (II) photoreduction process did not happen again (Yan, et al., 2020).

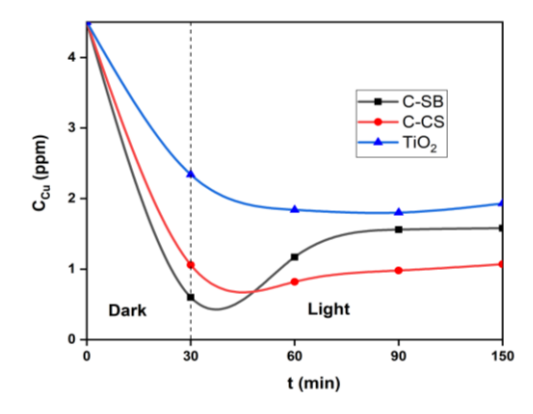


Figure 4: Photocatalysis process Cu (II) with different kinds of catalyst

The concentration of Cu (II) in the solution using the C-CS catalyst tends to increase in the following minutes. This occurs because the degradation process has not happened entirely, where the expected final result is Cu 0 . However, because the number of electrons or superoxide radicals produced is limited, the resulting degradation of Cu (II) is still Cu $^{+}$. This ion formation reaction is reversible, so when the amount of Cu $^{+}$ produced is more than the number of electrons or superoxide radicals, the ion will tend to release electrons (reoxidation), and Cu (II) is formed again and causes its concentration in the solution increases (Chemistry, et al., 2002).

$$Cu^{2+} + e^- \to Cu^+ \tag{7}$$

$$Cu^{2+} + O_2^- \bullet \to Cu^+ + O_2$$
 (8)

$$2Cu^+ \leftrightarrow Cu^{2+} + Cu^0 \tag{9}$$

The decrease in Cu (II) concentration during the photocatalytic process did not even occur when using a C-SB catalyst. This happens because a large amount of Cu (II) adsorbed causes the active site on the rGO surface to be fully charged, so there is no empty active site to attract the remaining Cu (II) in the solution or to attract the electrons from TiO_2 conduction band. The saturated condition on the active site of rGO causes desorption, and the Cu (II) concentration increases during irradiation.

TiO₂'s role as an electron producer is not seen during the UV irradiation. According to Liu et al., it is possible that TiO2 agglomeration can occur in the synthesis process (Liu, et al., 2013). Another cause is that the electrons generated tend to re-combine with holes in the valence band due to the improper role of rGO or the absence of a hole scavenger during the photocatalytic process. In Yan et.al's study, the decrease in Cu (II) concentration did not occur during the photocatalytic process. This event occurs when adding a hole scavenger in solution is not carried out (Yan, et al., 2020). This hole scavenger is a compound such as EDTA or formic acid that is intentionally added to inhibit the recombination process of electron holes in Cu photoreduction. The hole scavenger will generate electrons that directly fill the valence band, thereby inhibiting electron-hole recombination, and electrons in the conduction band are still available to reduce Cu (II) (Aman, et al., 2011). The equation for the formation of electron holes by TiO₂ when exposed to UV light and the recombination reaction between holes and electrons that occurs quickly after the electron-hole pair is formed is presented as follows(31):

$$TiO_2 \stackrel{hv}{\rightarrow} e_{CB}^- + h_{VB}^{+} \tag{10}$$

$$e_{CB}^{-} + h_{VB}^{+} \to heat \tag{11}$$

3.3 Photocatalysis for organic pollutants removal

To determine the role of rGO in the photodegradation process of organic pollutants, the composites synthesized with the addition of rGO from bagasse (C-SB) and coconut shell (C-CS) are used as photocatalysts in a solution containing MB. The initial concentration of MB used was 5 ppm. The total reaction time is 150 minutes, consisting of 30 minutes for the adsorption process and 120 minutes for the photocatalytic process. The catalyst concentration used was 1 g / L. The photocatalytic process begins by placing the solution on a magnetic stirrer in a dark room for 30 minutes so that the adsorption and equilibrium process occurs. Based on Figure 5, the presence of rGO in the composite increases the adsorption of MB compared to TiO_2 alone.

The adsorption ability in the presence of rGO in the composites was quite good because the MB concentration decreased by 40% for C-CS and 44% for C-SB from the initial concentration. Meanwhile, ${\rm TiO_2}$ in dark conditions

can only reduce the concentration of MB by 27%. In the MB adsorption process by rGO, the main interaction that occurs is the π - π interaction between the rGO aromatic ring and MB and partly an electrostatic interaction between the negative charge of the oxygen group on the rGO surface and the positive charge of the amino group on MB (Ma, et al., 2014; Kim, et al., 2015; Akrami, et al., 2019).

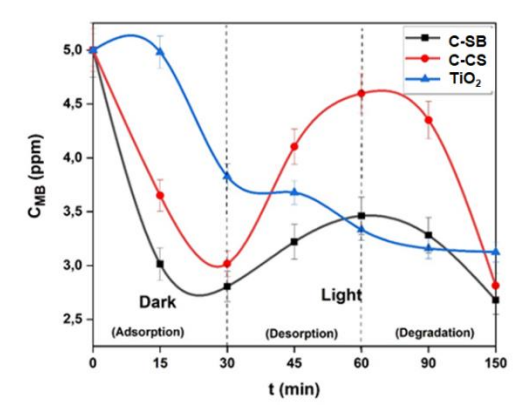


Figure 5: Photocatalysis process MB with different kinds of catalyst

At the beginning of the photocatalytic process where after 30 minutes of irradiation, the phenomenon that occurs is an increase in the concentration of MB. This indicates the desorption of MB from the surface of the catalyst. This event occurs due to the physical properties of adsorption, where the molecules of MB tend to return to the solution after equilibrium has been reached (Sharma, et al., 2013). This increase in concentration can also be caused by the adsorption process that occurs dominated by the interaction of π - π the rGO aromatic ring interface and MB. The decreasing of the oxygen functional group in rGO, makes the aromatic structure to be formed properly so that the main component of rGO is the C-C or C = C bond which is rich in π electrons. π - π interactions can occur through π electrons localized in aromatic rings conjugated in rGO and MB (Kim, et al., 2015). The π - π interaction is a non-covalent interaction with a weak bond energy, is reversible, and is easily influenced by external effects (Fessenden, 1986). With the irradiation, TiO₂ begins to react and produce electrons. The transfer of electrons from the conduction band TiO_2 to the rGO surface can disturb the stability of the π - π interaction between rGO and MB which can cause the interaction of the two molecules to break. This results in MB being dissolved again in the solution so that the concentration has increased (Deng, et al., 2020).

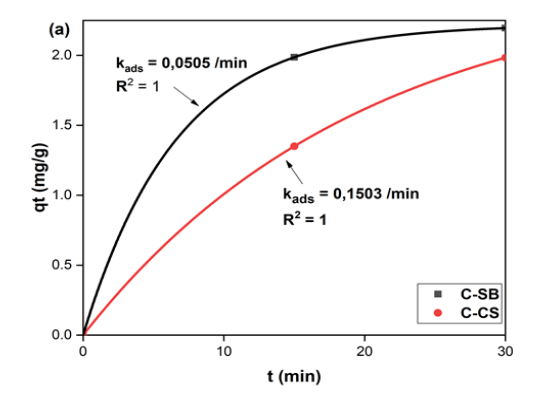
The decrease in the concentration of MB in the photocatalytic process only occurred after the next 30 minutes of irradiation. The decrease was 39% for C-CS and 23% for C-SB when calculated from the concentration of MB after an increase in concentration in the previous 30 minutes. From the whole process, both after the adsorption, desorption, and photocatalytic processes, the concentration of MB decreased by 44% for C-CS and 46% for C-SB. The photodegradation of MB using TiO2-rGO composites from coconut shell or bagasse as a photocatalyst has not shown optimal results due to: (i) TiO2 is unevenly distributed on the rGO surface and tends to agglomerate during the synthesis process. This is also reinforced by the SEM results which show TiO2 forms a larger size which indicates a agglomeration process; (ii) oxidant radicals have a short life time so that the degradation process of MB by oxidant radicals only lasts a short time so that not all of the MB can be degraded; (iii) there are still pairs of holes and electrons that reunite so that electrons that should leave the conduction band or holes that come out of the valence band to react with O2 or H2O to form radicals are not maximal so that the degraded MB is not optimal (Kusiak-Neiman, et al., 2020; Liu, et al., 2011).

3.4 Kinetics of adsorption-photocatalytic reactions

Catalyst addition in C-CS and C-SB does not affect the Cu (II) photoreduction process. As for MB, the photodegradation process is preceded by the presence of an adsorption process in dark conditions and desorption in the first 30 minutes of irradiation, so that the reaction kinetics will be applied in the entire photodegradation process of MB which includes the adsorption, desorption and photodegradation processes.

The adsorption capacity of a catalyst has a fairly important effect on the performance of photocatalysis, so an assessment of the adsorption capacity of the catalyst against MB at room temperature and in dark conditions is necessary. The effect of adding rGO in the composites is shown in Figure 4, where in dark conditions, both C-CS and C-SB composites show better adsorption capacity than TiO₂. The adsorption capacity in equilibrium conditions (q_e) and the adsorption rate constant (k_{ads}) in this process are estimated using the pseudo-first-order non-linear and pseudo-second-order linear models. As for measuring the suitability of the proposed model, it is based on the value of R^2 and the suitability of the phenomena. Equations (2) and (3) are used to obtain the value of the adsorption rate constant (k_{ads}) and the adsorption capacity in equilibrium conditions (q_e). In this equilibrium system, adsorption and desorption have equal rates and have been included in the calculations as driving forces.

Table 1: Kinetics parameters of MB adsorption									
	qe exp (mg/g)	Pseudo Order 1			Pseudo Order 2				
Catalyst		k _{ads} (1/min)	qe (mg/g)	R ²	k _{ads} (g/mg.min)	qe (mg/g)	R ²		
C-SB	2.19	0.0505	2.54	1	0.8689	2.19	0.9963		
C-CS	1.98	0.1503	2.22	1	0.2150	1.98	0.9317		



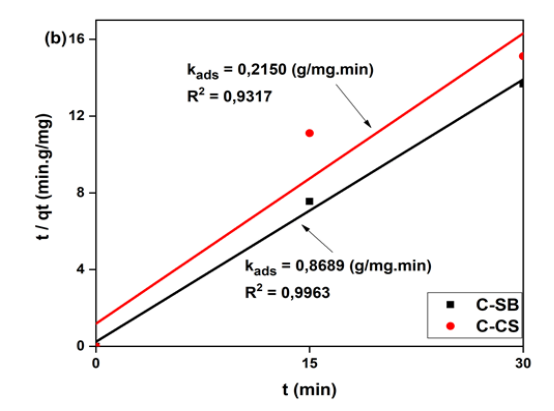


Figure 6: Adsorption curve of MB (a) pseudo-first-order (b) pseudo-second-order

The kinetics of the adsorption rate of MB is more suitable to be described by the pseudo-first-order model when seen from the higher correlation coefficient as shown in Table 1 and Figure 6. R² in the pseudo-first-order has a value equal to one, while the pseudo-second-order model shows a variable and is lower when compared to the pseudo first-order. However,

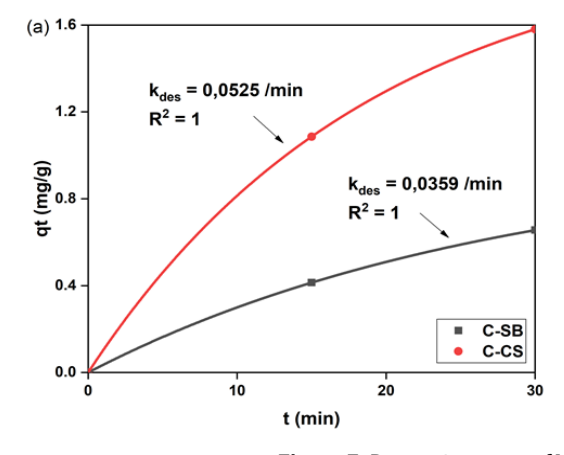
based on the phenomena as shown in Figure 5, where at the same time, C-SB catalyst can adsorb more MB, then the pseudo second order model is more suitable to describe the reaction phenomenon that occurs. This is indicated by the adsorption rate constant obtained from the calculation, where C-SB has value four times greater than C-CS, which means that C-SB

can adsorb MB faster than C-CS.

In the desorption process, the desorption rate constants (k_{des}) and the desorption capacity under equilibrium (q_{e}) are also estimated using the pseudo first-order and second order. The model chosen is based on the correlation coefficient value (R^2) and considers its suitability with the phenomenon that occurs. According to the kinetics parameters shown in

Table 2 and Figure 7, the first-order pseudo model is more suitable for describing the kinetics of the MB desorption reaction, as evidenced by the value of the correlation coefficient (R²) equal to one. The desorption rate constants obtained from the calculation also illustrate the suitability of the phenomenon that occur as shown in Figure 5, where the C-CS catalyst has desorption ability on MB faster than the C-SB which is shown with a $k_{\rm des}$ value that is 1,4 times greater.

Table 2: Kinetics parameters of MB desorption									
	qe _{exp} (mg/g)	Pseudo Order 1			Pseudo Order 2				
Catalyst		k _{des} (1/min)	qe (mg/g)	R ²	k _{des} (g/mg.min)	qe (mg/g)	R ²		
C-SB	0.66	0.0359	0.99	1	0.5225	0.66	0.8980		
C-CS	1.58	0.0525	1.99	1	0.2780	1.58	0.9354		



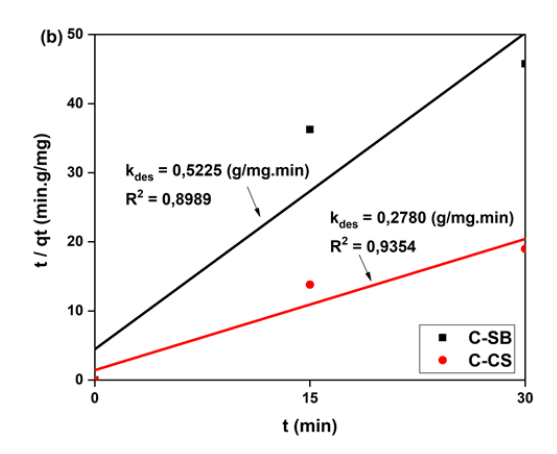


Figure 7: Desorption curve of MB (a) pseudo-first-order (b) pseudo-second-order

Photodegradation - the first-order L-H model is widely used to describe the photodegradation of MB. Nguyen-Phan et al reported on the photodegradation of MB by varying the addition of GO to the TiO₂-GO synthesis followed by a first-order reaction (Nguyen-Phan, et al., 2011). Wu et al. reported the photodegradation of MB by TiO₂-graphene with UV radiation which was also followed by first-order reaction kinetics (Wu, et al., 2014). A similar thing was also reported by Kusiak-Nejman et al, where first-order reaction kinetics were used to describe the decomposition of MB in hybrid TiO₂-rGO photocatalysts (Kusiak-Nejman, et al., 2020).

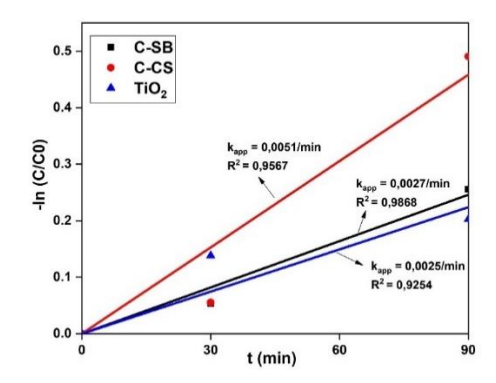


Figure 8: Linear curve photodegradation kinetics of MB

The photodegradation of MB using C-CS and C-SB catalysts shows a greater reaction rate constant compared to TiO_2 as shown in Figure 8. The reaction rate constant of the C-CS catalyst has a value two times greater than that of TiO_2 . The addition of rGO in the photocatalyst influences the photodegradation of MB. The functions of rGO in the photocatalytic process include as an adsorbent to accelerate the MB adsorption process, an electron acceptor that accelerates the transfer of electrons from the TiO_2 conduction band, thereby inhibiting electron-hole recombination and functioning as an absorber so that light will more easily reach to TiO_2 surface, thereby accelerating the process of forming electron-hole pairs (Nguyen-Phan, et al., 2011).

According to experimental observations, when light radiation is present,

the adsorption equilibrium continuously shifts toward the desorption side, meaning the percentage of adsorbed methylene blue is always declining. For simplicity's sake, it is assumed that the net desorption rate is first order concerning the amount of methylene blue adsorbed on the catalyst's surface. Thus, the data obtained from the experiment were also tested using the following equation (Xu, et al., 2014):

$$\frac{dC_a}{dt} = -k_{des}C_a \tag{12}$$

where Ca is the concentration of MB adsorbed on the surface of the catalyst (g / g of catalyst), k_{des} is the constant rate of the desorption reaction (min⁻¹).

The concentration of MB adsorbed on the surface of the catalyst can also be written with the following equation:

$$C_a = C_{a0} \exp(-k_{des}t) \tag{13}$$

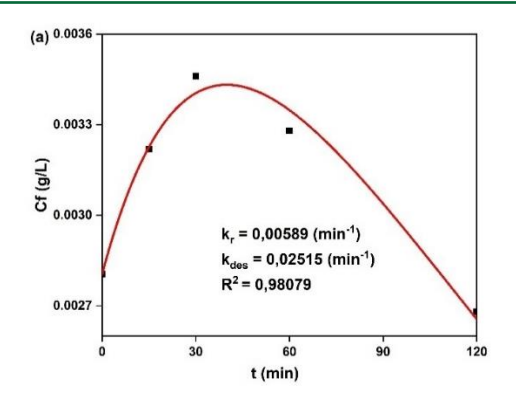
where C_{a0} is the concentration of MB adsorbed at the beginning of irradiation (g/L). Due to both desorption and degradation processes, the concentration of "free" methylene blue in the solution has changed and follow the equation:

$$\frac{dC_f}{dt} = -r - \frac{dC_a}{dt} = \frac{1}{V} \left[-k_r C_f V + k_{des} C_a C_s V \right]$$
(14)

 C_f is the concentration of MB in solution (g/L), k_r is the constant rate of the degradation reaction (min⁻¹), V is the volume of solution (L), C_s is the concentration of catalyst (g/L) and r is the degradation reaction rate. The net change in the concentration of adsorbed methylene blue, or the rate of adsorption less the rate of desorption, is the second term in equation 14. It consists of two parts, the first part describes the effect of degradation, and the second part describes the shift adsorption and desorption equilibrium, where the solution can be written as the following equation:

$$C_f = \frac{k_{des}}{k_r - k_{des}} C_s C_{a0} \exp(-k_{des} t) + \left[C_{f0} - \frac{k_{des} C_s C_{a0}}{k_r - k_{des}} \right] \exp(-k_r t)$$
 (15)

 C_{f0} is the initial concentration of MB in solution at the beginning of irradiation (g/L). The rate constants for desorption and degradation reactions can be calculated using non-linear equations via the OriginProsoftware



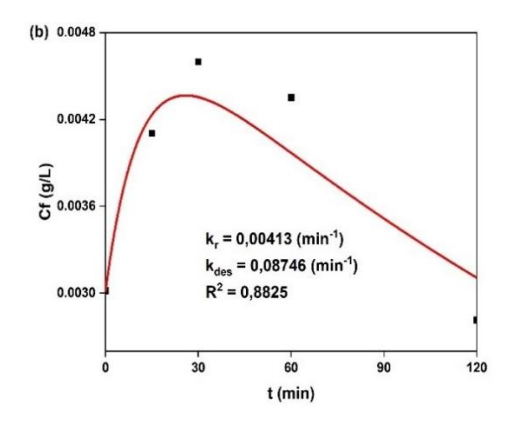


Figure 9: The curve of non-linear reaction kinetics of degradation and desorption of photocatalytic MB on catalyst (a) C-SB (b) C-CS

According to the graph shown in Figure 9, it can be seen that the reaction kinetics model for the degradation and desorption processes shows a correlation coefficient (R^2) of 0.98079 for C-SB catalyst and 0.8825 for C-CS. The degradation rate constant (k_1) on the C-SB shows a greater value than C-CS. On the other hand, for the MB desorption rate constant (k_2), the

C-CS catalyst has a greater value, compared to C-SB. The desorption and degradation reaction kinetics parameters obtained from first order, pseudo first order, or the model proposed can be seen in Table 3 (Xu et al., 2014).

Table 3: Kinetics parameters of MB desorption and degradation were obtained from different reaction kinetics models									
	Reaction Kinetics Model								
0.1.	Pseudo First Order		First Order		Xu et.al				
Catalyst	Desorption		Degradation		Desorption		Degradation		
	k _{des}	R ²	k _{app}	R ²	k _{des}	R ²	$k_{\rm r}$	R ²	
C-SB	0.0359	1	0.0027	0.9868	0.0252	0.9807	0.0059	0.9807	
C-CS	0.0525	1	0.0051	0.9567	0.0875	0.8825	0.0041	0.8825	

Based on the data above, the values obtained can be grouped and presented more simply to compare which model is more suitable for use, as shown in Tables 4 and 5.

Table 4: Comparison of reaction rate constant values of different reaction kinetics models								
Reaction Rate Constant								
	Desoi	rption	Degradation					
Kinetic Model	C-SB	C-CS	C-SB	C-CS				
Pseudo First Order	0.0359	0.0525	-	-				
First Order	-	-	0.0027	0.0051				
Xu et al	0.0252	0.0875	0.0059	0.0041				

Table 5: Percentage of the suitability of \mathbb{R}^2 values from different reaction kinetics models								
Suitability of R ² Values								
Kinetic Model	Desor	rption	Degradation					
Kinetic Model	C-SB (%)	C-CS (%)	C-SB (%)	C-CS (%)				
Pseudo First Order	100	100	-	-				
First Order	-	-	98.68	95.67				
Xu et al	98.07	88.25	98.07	88.25				

According to the data shown in Table 4, the desorption reaction rate constants obtained from the pseudo-order kinetics, or the concept proposed by Xu et al., both on C-SB and C-CS catalysts, did not show significant differences in values. Both models show that the rate constant of the desorption for the C-CS catalyst is greater than C-SB, which means that C-CS can desorb MB faster than the C-SB catalyst. This phenomenon matches with the phenomenon in the desorption process shown in Figure

5, where at the same time the C-CS catalyst can desorb more MB than C-SB

Whereas in the degradation rate constant, the values obtained from the two models for both C-SB and C-CS catalysts show different phenomena. For the first-order kinetics model, C-CS catalyst was able to degrade MB faster than C-SB, which was indicated by the value of C-CS reaction rate constant being greater than C-SB. A different thing is shown in the kinetics

model according to the concept conveyed by Xu et.al., where C-SB has a degradation rate constant value greater than C-CS. Based on the phenomena that occur during the research as shown in Figure 5, the first-order model describes the real conditions of the MB degradation process, where the C-CS catalyst can degrade MB faster than the C-SB.

To further ascertain which model is more suitable, the correlation coefficients of the two models are compared and selected based on R^2 values that are close to one or have a 100% conformity percentage. According to the data shown in Table 5, it can be seen that the pseudoorder model shows 100% suitability in the desorption process for the two types of catalysts. As for the degradation process with the first-order model, C-SB showed compatibility with the R^2 value of 98.68%, and C-CS was 95.67%. Whereas for the kinetics model proposed by Xu et al., one type of catalyst produces the same R^2 value in the desorption and

degradation processes. In using C-SB as a catalyst, the R^2 value for both the desorption and degradation processes resulted in a suitability of the R^2 value of 98,07%. Meanwhile, the C-CS catalyst showed suitability only 88,25% for desorption and degradation. So based on the data above, pseudo-order is a more suitable model for desorption and a first-order model for degradation of MB using C-SB and C-CS as photocatalysts. The processes that occur in this experiment as a whole include adsorption, desorption and degradation. In dark conditions, the adsorption process takes place until equilibrium occurs where the rate of adsorption equals the rate of desorption. The adsorption rate constant on the C-BS sample shows a value of 0.0505/min with an adsorption capacity at equilibrium of 2.54 mg/g. While the desorption rate constant on the same sample is 0.0359/min with a desorption capacity at equilibrium of 0.99 mg/g. If the two phenomena are compared, it is seen that the adsorption process occurs faster than the desorption process.

Table 6: Relationship of adsorption, desorption, and maximum capacity at equilibrium							
Sample		Xu et al.					
	qe _(ads)	k _{ads}	qe _(des)	\mathbf{k}_{des}	\mathbf{k}_{des}		
C-SB	2.54	0.0505	0.99	0.0359	0.0252		
C-CS	2.22	0.1503	1.99	0.0525	0.0875		

The processes that occur in this experiment as a whole include adsorption, desorption, and degradation. The relationship of adsorption, desorption, and maximum capacity at equilibrium is shown in Table 6. In dark conditions, the adsorption process occurs until equilibrium occurs, where the adsorption rate equals the desorption rate. The adsorption rate constant on the C-SB shows a value of 0.0505/min with an adsorption capacity at an equilibrium of 2.54 mg/g. (The adsorption referred to here also involves desorption, but the adsorption is more dominant). In the bright condition, the desorption rate constant on the same sample is 0.0359/min with a maximum capacity at equilibrium of 0.99 mg/g (The desorption referred to here also involves adsorption, but the desorption process is more dominant). If the two phenomena are compared, it is seen that adsorption (dark conditions) occurs faster than the desorption process (bright conditions). This is evidenced by the value of kads being greater than k_{des} using the pseudo-first-order and the Xu et al. model. When equilibrium occurs where the adsorption and desorption rates are the same (in dark conditions), the maximum adsorption capacity is 2.54 mg/g. This value exceeds the maximum adsorption capacity in bright conditions, only 0.99 mg/g. The relationship of adsorption, desorption, and maximum capacity at equilibrium in C-CS is also the same as C-SB, where the adsorption rate in dark conditions is greater than the desorption rate in light conditions, as is the maximum adsorption capacity.

CONCLUSIONS

The characterization results by SEM and XRD tests show that the $rGO-TiO_2$ composite has been successfully synthesized using the hydrothermal method. The rGO used is derived from sugarcane bagasse and coconut shell. The results demonstrate that the TiO2-rGO composite derived from sugarcane bagasse can remove up to 87% of Cu(II) and degrade 46% of methylene blue (MB), while the composite from coconut shell achieved Cu(II) removal of 76% and MB degradation of 44%. The rGO component plays a key role in Cu(II) removal through a dominant adsorption mechanism, whereas TiO2 contributes significantly to the photocatalytic degradation of MB. The composites exhibit effective degradation of organic pollutants after an initial adsorption-desorption phase, while for inorganic Cu(II), the process is dominated by adsorption, with limited photoreduction. The photocatalytic degradation of MB is best described by a first-order kinetics model, as evidenced by the calculated rate constants and strong correlation coefficients (R2). These findings indicate the potential application of agricultural waste-derived rGO-TiO2 composites as cost-effective and sustainable materials for integrated wastewater treatment, contributing to pollutant removal and water resource conservation in environmental management.

ACKNOWLEDGMENTS

Authors acknowledged Deputy for Strengthening Research and Development, National Research and Innovation Agency, Indonesia for the research financial support No: 187-08/UN7.6.1/PP/2022 and World Class University Program 2023 Universitas Diponegoro, Indonesia for the mobility funding support.

FUNDING AND/OR CONFLICTS OF INTERESTS/COMPETING INTERESTS

All authors certify that they have no affiliations with or involvement in any organization or entity with any financial interest or non-financial interest in the subject matter or materials discussed in this manuscript. The authors have no financial or proprietary interests in any material discussed in this article.

REFERENCES

- Akrami, M., Danesh, S., and Eftekhari, M., 2019. Comparative study on the removal of cationic dyes using different graphene oxide forms, Pp.1785–1797.
- Aman, N., Mishra, T., Hait, J., and Jana, R. K., 2011. Simultaneous photoreductive removal of copper (II) and selenium (IV) under visible light over spherical binary oxide photocatalyst. Journal of Hazardous Materials, 186(1), Pp. 360–366.
- Ariyanti, D., Lesdantina, D., Budiyono, and Satriadi, H., 2021. Synthesis and characterization of graphene-like material derived from sugarcane bagasse. IOP Conference Series: Materials Science and Engineering, 1053(1), 012013.
- Ariyanti, D., Lesdantina, D., Purbasari, A., and Astuti, Y., 2023. Synthesis of graphene-like material derived from biomass from agricultural waste and its application in Cu (II) removal. Korean Journal of Chemical Engineering.
- Ariyanti, D., Lesdantina, D., Purbasari, A., Saputro, A., and Gao, W., 2022. Sedimentation process of TiO_2 nanoparticles in aqueous solution. Reaktor, 22(2), Pp. 70–76.
- Ariyanti, D., Maillot, M., and Gao, W., 2017. TiO₂ used as photocatalyst for rhodamine B degradation under solar radiation. International Journal of Modern Physics B, 1744095. https://doi.org/10.1142/S0217979217440957
- Ariyanti, D., Maillot, M., and Gao, W., 2018. Photo-assisted degradation of dyes in a binary system using $\rm TiO_2$ under simulated solar radiation. Journal of Environmental Chemical Engineering, 6(1), Pp. 539–548. https://doi.org/10.1016/j.jece.2017.12.031
- Baorang, L., Xiaohui, W., Minyu, Y., and Longtu, L., 2002. Preparation and characterization of nano- TiO_2 powder. Materials Chemistry and Physics, 78(1), Pp.184–188.
- Baqiya, M. A., Nugraheni, A. Y., Islamiyah, W., Kurniawan, A. F., Ramli, M. M., Yamaguchi, S., 2020. Structural study on graphene-based particles prepared from old coconut shell by acid-assisted mechanical exfoliation. Advanced Powder Technology, 31(5), Pp. 2072–2078.
- Burakov, A. E., Galunin, E. V., Burakova, I. V., Kucherova, A. E., Agarwal, S., Tkachev, A. G., 2018. Adsorption of heavy metals on conventional and nanostructured materials for wastewater treatment purposes: A review. Ecotoxicology and Environmental Safety, 148, Pp. 702–712.
- Chaabane, L., Beyou, E., El Ghali, A., and Baouab, M. H. V., 2020.

- Comparative studies on the adsorption of metal ions from aqueous solutions using various functionalized graphene oxide sheets as supported adsorbents. Journal of Hazardous Materials, 389, 121839.
- Chemistry, P., and Demokritos, N., 2002. Photocatalytic reduction and recovery of copper by polyoxometalates. Journal Name, 36(24), Pp. 5355–5362.
- Deng, J. H., Luo, J., Mao, Y. L., Lai, S., and Gong, Y. N., 2020. π-π stacking interactions: Non-negligible forces for stabilizing porous supramolecular frameworks, 1(January), Pp. 1–9.
- Ding, S., Sun, S., Xu, H., Yang, B., Liu, Y., and Wang, H., 2019. Preparation and adsorption property of graphene oxide by using waste graphite from diamond synthesis industry. Materials Chemistry and Physics, 221(100), Pp. 47–57.
- Emiru, T. F., and Ayele, D. W., 2017. Controlled synthesis, characterization and reduction of graphene oxide: A convenient method for large scale production. Egyptian Journal of Basic and Applied Sciences, 4(1), Pp. 74–79.
- Fessenden., 1986. Kimia Organik (3rd ed.). 56 p.
- Guerrero-Contreras, J., and Caballero-Briones, F., 2015. Graphene oxide powders with different oxidation degree, prepared by synthesis variations of the Hummers method. Materials Chemistry and Physics, 153, Pp. 209–220.
- Guerrero-Contreras, J., and Caballero-Briones, F., 2015. Graphene oxide powders with different oxidation degree, prepared by synthesis variations of the Hummers method. Materials Chemistry and Physics, 153, Pp. 209–220. https://www.sciencedirect.com/science/article/pii/S02540584150 00061
- Kim, G. A. K. R. T. S. V. G. S. J., 2015. Removal of heavy metal ions from pharma-effluents using graphene-oxide nanosorbents and study of their adsorption kinetics. Journal of Industrial and Engineering Chemistry.
- Kim, H., Kang, S. O., Park, S., and Park, H. S., 2015. Adsorption isotherms and kinetics of cationic and anionic dyes on three-dimensional reduced graphene oxide macrostructure. Journal of Industrial and Engineering Chemistry, 21, Pp. 1191–1196.
- Kusiak-Nejman, E., Wanag, A., Kapica-Kozar, J., Kowalczyk, Ł., Zgrzebnicki, M., Tryba, B., 2020. Methylene blue decomposition on TiO₂/reduced graphene oxide hybrid photocatalysts obtained by a two-step hydrothermal and calcination synthesis. Catalysis Today, 357, Pp. 630–637.
- Lee, X. J., Hiew, B. Y. Z., Lai, K. C., Lee, L. Y., Gan, S., Thangalazhy-Gopakumar, S., 2019. Review on graphene and its derivatives: Synthesis methods and potential industrial implementation. Journal of the Taiwan Institute of Chemical Engineers, 98, Pp. 163–180.
- Lesdantina, D., and Ariyanti, D., 2020. Graphene and graphene oxide: Raw materials, synthesis, and application. AIP Conference Proceedings, 2197(1). https://doi.org/10.1063/1.5140916
- Li, B., Jin, X., Lin, J., and Chen, Z., 2018. Green reduction of graphene oxide by sugarcane bagasse extract and its application for the removal of cadmium in aqueous solution. Journal of Cleaner Production, 189, Pp. 128–134.
- Liu, J., Wang, Z., Liu, L., and Chen, W., 2011. Reduced graphene oxide as capturer of dyes and electrons during photocatalysis: Surface wrapping and capture promoted efficiency. Physical Chemistry Chemical Physics, 13(29), Pp. 13216–13221.
- Liu, S., Sun, H., Liu, S., and Wang, S., 2013. Graphene facilitated visible light photodegradation of methylene blue over titanium dioxide photocatalysts. Chemical Engineering Journal, 214, Pp. 298–303.

- Ma, T., Chang, P. R., Zheng, P., Zhao, F., and Ma, X., 2014. Fabrication of ultra-light graphene-based gels and their adsorption of methylene blue. Chemical Engineering Journal, 240, Pp. 595–600.
- Muramatsu, H., Kim, Y. A., Yang, K. S., and Cruz-Silva, R., 2014. Rice husk-derived graphene with nano-sized domains and clean edges, Pp. 1–5.
- Nguyen-Phan, T. D., Pham, V. H., Shin, E. W., Pham, H. D., Kim, S., Chung, J. S., 2011. The role of graphene oxide content on the adsorption-enhanced photocatalysis of titanium dioxide/graphene oxide composites. Chemical Engineering Journal, 170(1), Pp. 226–232.
- Peter, A., Indrea, E., Nicula, C., Tutu, H., and Bakatula, E., 2012. Dual efficiency of nano-structured TiO₂/zeolyte systems in removal of copper (II) and lead (II) ions from aqueous solution under visible light. [Journal name missing], 143(II), Pp. 139–143.
- Seekaew, Y., Arayawut, O., Timsorn, K., and Wongchoosuk, C., 2018. Synthesis, characterization, and applications of graphene and derivatives. In Carbon-Based Nanofillers and Their Rubber Nanocomposites (pp. 259–283). Elsevier Inc.
- Sharma, M., Behl, K., Nigam, S., and Joshi, M., 2018. TiO₂–GO nanocomposite for photocatalysis and environmental applications: A green synthesis approach, 156(August), Pp. 434–439.
- Sharma, P., Hussain, N., Borah, D. J., and Das, M. R., 2013. Kinetics and adsorption behavior of the methyl blue at the graphene oxide/reduced graphene oxide nanosheet–water interface: A comparative study.
- Sujiono, E. H., Zurnansyah, Zabrian, D., Dahlan, M. Y., Amin, B. D., Samnur., 2020. Graphene oxide based coconut shell waste: Synthesis by modified Hummers method and characterization. Heliyon, 6(8), e04568.
- Tomczyk, A., Sokołowska, Z., and Boguta, P., 2020. Biomass type effect on biochar surface characteristic and adsorption capacity relative to silver and copper. Fuel, 278, 118317. https://doi.org/10.1016/j.fuel.2020.118317
- Wu, Z., Zhang, L., Guan, Q., Ning, P., and Ye, D., 2014. Preparation of α-zirconium phosphate-pillared reduced graphene oxide with increased adsorption towards methylene blue. Chemical Engineering Journal, 258, Pp. 77–84. https://doi.org/10.1016/j.cej.2014.07.061
- Xu, C., Rangaiah, G. P., and Zhao, X. S., 2014. Photocatalytic degradation of methylene blue by titanium dioxide: Experimental and modeling study. Industrial and Engineering Chemistry Research, 53(38), Pp. 14641–14649. https://doi.org/10.1021/ie5006015
- Yan, R., Luo, D., Fu, C., Tian, W., Wu, P., Wang, Y., 2020. Simultaneous removal of Cu(II) and Cr(VI) ions from wastewater. Journal of Water Process Engineering, 33, 101005. https://doi.org/10.1016/j.jwpe.2019.101005
- Yu, B., Zhang, Y., Shukla, A., Shukla, S. S., and Dorris, K. L., 2000. The removal of heavy metal from aqueous solutions by sawdust adsorption: Removal of copper. Journal of Hazardous Materials, 80(1– 3), Pp. 33–42. https://doi.org/10.1016/S0304-3894(00)00278-8
- Zhang, H., Lv, X., Li, Y., Wang, Y., and Li, J., 2010. P25-graphene composite as a high performance photocatalyst. ACS Nano, 4(1), Pp. 380–386. https://doi.org/10.1021/nn901221k
- Zhang, X., Zhang, D. C., Chen, Y., Sun, X. Z., and Ma, Y. W., 2012. Electrochemical reduction of graphene oxide films: Preparation, characterization and their electrochemical properties. Chinese Science Bulletin, 57(23), Pp. 3045–3050. https://doi.org/10.1007/s11434-012-5307-1
- Zhang, Y., Tan, Z. R., 2010. ${\rm TiO_2-graphene}$ nanocomposites for gas-phase photocatalytic degradation of volatile aromatic pollutants. Journal of Materials Chemistry, 20(29), Pp. 5786–5794. https://doi.org/10.1039/c0jm00085j

